# Statistical Modeling of Ultrawideband MIMO Propagation Channel in a Warehouse Environment

Sangodoyin, Seun; Kristem, Vinod; Molisch, Andreas F.; He, Ruisi; Tufvesson, Fredrik; Behairy, Hatim Mohammed

*Published in:*
IEEE Transactions on Antennas and Propagation

*DOI:*
10.1109/TAP.2016.2583477

2016

*Document Version:*
Peer reviewed version (aka post-print)

# Statistical Modeling of Ultrawideband MIMO Propagation Channel in a Warehouse Environment

Seun Sangodoyin, *Student Member, IEEE*, Vinod Kristem, *Student Member, IEEE*, Andreas F. Molisch, *Fellow, IEEE*, Ruisi He, *Member, IEEE*, Fredrik Tufvesson, *Senior Member, IEEE*, Hatim Behairy, *Member, IEEE*

***Abstract*—This paper describes an extensive propagation channel measurement campaign in a warehouse environment for Line-of-sight (LOS) and Non-Line-of-sight (NLOS) scenarios. The measurement setup employs a vector network analyzer (VNA) operating in the 2–8 GHz frequency band combined with an 8 x 8 virtual multiple-input-multiple-output (MIMO) antenna array. We develop a comprehensive statistical propagation channel model based on high-resolution extraction of multipath components (MPCs), and subsequent spatio-temporal clustering analysis. The *intra*-cluster Direction of Departure (DoD), Direction of Arrival (DoA) and the Time of Arrival (ToA) are independent, both for the LOS and NLOS scenarios. The intra-cluster DoD and DoA can be approximated by the Laplace distribution, and the intra-cluster ToA approximated by an exponential mixture distribution. The *inter*-cluster analysis however, shows a dependency between the cluster DoD, DoA and ToA. To capture this dependency, we separately model the clusters caused by single and multiple bounce scattering along the aisles in the warehouse. The inter-cluster DoD distribution follows a Laplace distribution, while the cluster DoA conditioned on the DoD is approximated by a Gaussian mixture distribution. The model was validated using the capacity and delay-spread values.**

***Index Terms*—Propagation channel, ultra-wideband (UWB), MIMO, statistical channel model, warehouse environment**

## I. Introduction

Ultra-wideband (UWB) technology has emerged as one of the most promising candidates for communication and localization systems and has attracted great interest from the scientific, military and industrial communities [1]–[4]. UWB signals are defined as either having more than 20% relative bandwidth or more than 500 MHz absolute bandwidth [5] and are permitted to operate in the 3.1–10.6 GHz frequency band by the Federal Communication Commission (FCC) [6] in the USA, while occupying 4.2–4.8 GHz and 6–8.5 GHz band in Europe, according to the European conference of postal and telecommunications Administrations (CEPT) and 3.4 – 4.8 GHz, 7.25 – 10.25 GHz bands in Japan. UWB signals show a number of important and attractive qualities such as, accurate position location and ranging due to its fine time resolution [7], [8], robustness to frequency-selective fading [1], [9], possibility of extremely high data rates for communications [10], efficient use of radio spectrum through underlaying techniques [11] and easier material penetration due to the presence of energy at different frequencies. Ultra-wideband systems have many envisioned applications including real-time tracking of assets, personnel and hospital patients and could especially be of great use in locating items in a warehouse environment. For example, UWB as-of-late has found use in Radio-frequency identification (RFID) technology, which is naturally deployed in warehouse environment, and in UWB-based wireless sensor networks, which could eventually find use in a warehouse-like environment as well.

The warehouse environment is unique in its geometric/structural layout, which is often sparse with storage racks or shelves all demarcated into aisles. This constitutes a unique propagation channel, whose properties need to be explored for system design and simulation purposes.

### A. Related work

UWB systems are being designed to operate in different environments and as such channel models have been provided for several environments ranging from indoor–residential [12]–[15] to offices [16], factories or industrial [17], [18] and outdoor environment [19]–[22]. However, there is a dearth of propagation channel models for warehouse environments in the literature. In fact, to the best knowledge of the authors, there are hardly any channel models dealing with warehouse environments. Channel measurements were conducted in a warehouse environment in [23], however, the results provided were only for a single-input-single-output (SISO) channel model. Ref. [24], deals with channel models in the frequency range from 0.5 to 1.5 GHz, intended for UHF RFID systems at a warehouse portal. A warehouse channel measurement was also done in [25] to enhance a ray-tracing tool, but the measurements was only performed for 0.8–2.5 GHz.

### B. Contributions

In this paper, we remedy this gap by investigating the propagation channel parameters in a typical warehouse environment. The contributions of this paper can be summarized as follows:

- We report the details of a MIMO channel measurement campaign performed in a warehouse environment for a LOS and NLOS scenario in the 2–8 GHz frequency range.

Part of this work has appeared in International Conference on Communication (ICC), June, 2015. This work was financially supported in part by a National Science Foundation MRI grant, KACST and the DURIP (Defense University Research Instrumentation Program)

Seun Sangodoyin, Vinod Kristem and Andreas F. Molisch are with the Department of Electrical Engineering, University of Southern California (USC), Los Angeles, CA 90089-2560 USA. Ruisi He is with the Beijing Jiaotong Univ., Beijing, China. Fredrik Tufvesson is with the department of Electrical and information technology at Lund University, Sweden. Hatim Behairy is with KACST, Saudi Arabia. (Email: sangodoy@usc.edu; kristem@usc.edu; molisch@usc.edu; he.ruisi.china@gmail.com; Fredrik.Tufvesson@eit.lth.se; hbehairy@kacst.edu.sa)

- We extract the large scale propagation channel parameters such as distance-dependent path gain exponent ($n$), frequency-dependent path gain coefficient ($\kappa$) and shadowing variance ($\sigma^2$) for the LOS and NLOS environments.
- Using the high-resolution CLEAN algorithm, the temporal and directional parameters of the multipath components (MPCs) are extracted.
- In light of the observation that MPCs typically can be grouped into clusters corresponding to the scatterers and interacting objects (IO) in the environment, we performed a cluster analysis and derive both *intra-* and *inter-* cluster statistics.
- The inter-cluster DoA, DoD and ToA are observed to be dependent; and we develop a suitable model to capture this effect.
- The developed channel models are validated using capacity and root-mean-square (RMS) delay spreads as the validation metrics.

The developed model can be used for realistic performance evaluations of UWB systems in warehouse environments.

### C. Organization

The rest of the paper is organized as follows. Sec. II describes the measurement environment. Sec. III describes the measurement setup. The large scale parameter extraction is described in Sec. IV. The intra-cluster and inter-cluster channel models for LOS and NLOS environments is developed in Sec. V. The developed channel models are validated in Sec. VI.

## II. Measurement Environment

Measurements were performed at the University of Southern California (USC) main warehouse facility (shown in Fig. 1). The warehouse structure has four floors (including the basement) with each floor comprising of large open halls, which were mainly used for storing items such as books, computers and other office stationery. The ceiling, floor and walls surrounding each large open hall on each floor were made of reinforced bricks and concrete, while concrete pillars (labeled A in Fig. 1) served as structural supports for the ceiling (and could also contribute to shadowing effects in the propagation channel). Typically, the storage areas on each floor were often demarcated into aisles, with each aisle containing rows of two layered metallic storage racks (labeled B in Fig. 1). There also exists walkways/paths between these aisles to ease the movement of people and forklift trucks. To store sensitive material such as medical equipment or non-toxic laboratory chemicals, and old computer parts, special demarcations were made with barb-wired fences. Access to each storage hall is mainly through steel garage doors, which could serve as a source of reflections.

The measurements were conducted on the first floor and basement storage halls, see Figs. 2 & 3 for the floor plans. The use of the basement storage hall (with similar layout to the first floor, but with slightly different geometrical structures, i.e no concrete pillars or metallic garage doors) provided more measurement points, especially for large distance separations between transmitter (Tx) and receiver (Rx) ends.


Fig. 1. USC Warehouse Facility.

For both LOS and NLOS scenarios, measurements were taken for Tx-Rx separation distances of 5 m, 10 m, 15 m, 20 m and 25 m. Multiple measurements were taken for a given separation distance, by placing the Tx and Rx arrays at different positions. For each Tx-Rx separation distance, 5 and 8 positions were selected respectively for the LOS and NLOS scenarios. These positions provide different realizations of the shadowing effects and other distance-dependent large-scale effects. A total of 65 positions were measured in our campaign. The measured positions are indicated in the Figs. 2 & 3. The Tx/Rx array locations for the LOS/NLOS measurements are indicated on the floor maps with the abbreviations: TXL1 (Tx LOS position 1), TXN1 (Tx NLOS position 1), etc. A similar format is used for the Rx positions. To avoid congesting the floor schematic, only a subset of the measured positions are marked in the figures.

## III. Measurement Setup

A frequency domain channel sounder setup with an 8 x 8 virtual MIMO antenna array configuration (see Fig. 4) was used to perform the measurement campaign. At the heart of the channel sounder setup is a vector network analyzer (VNA, HP 8720ET) [26], which is used for obtaining the complex transfer function ($H(f)$) of the propagation channel. The VNA was calibrated with the inclusion of a 20 m long coaxial cable (to connect the Tx, Rx ends) rated at 1.22 dB/m at 8 GHz [27] and a 30 dB low noise amplifier (LNA) [28], which was used at the Rx to boost the received signal power. A stepped frequency sweep was conducted for 1601 points within the 2–8 GHz frequency range. The settings for the VNA are shown in Table I and a list of all equipment used is given in Table II.

The MIMO antenna array was implemented by using a *virtual* antenna array at both Tx and Rx. An omni-directional antenna [29] was attached to a 1.78 m high support pole and then fastened to a stepper motor controlled by linear positioner. Using a linear positioner controlled by LabView software, the single antenna was moved to different positions,

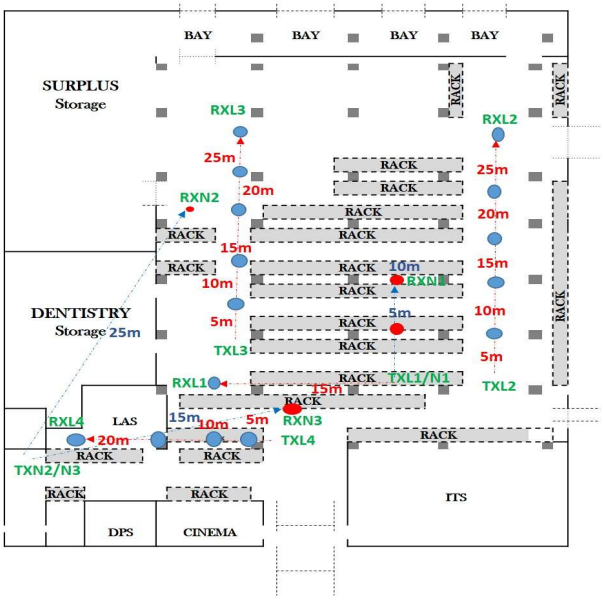


Fig. 2. Floor map of the first floor of the warehouse.

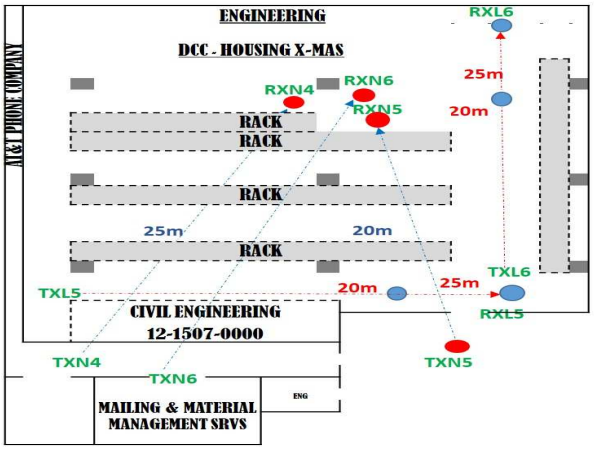


Fig. 3. Floor map of the basement of the warehouse.

thus creating a *virtual* uniform linear array (ULA), which allows determination of angular characteristics of the MPCs. Note, however, that a ULA does not allow extraction of the elevation of the MPCs, and the azimuth of MPCs incident from nonzero elevation is distorted. Due to the building structure, this effect did not play a major role. The separation between antenna elements is 50 mm, hence by moving each antenna over a distance of 400 mm at both ends, 8 antenna positions at each link end are measured, providing a total of 64 channel realizations. Due to array positioner movement time and VNA frequency sweep time (over a 6 GHz bandwidth), the total measurement time for each position (64 channels) was about 48 minutes. A key requirement for evaluations based on virtual arrays is that the channel is *static* during a measurement run. Several precautions were taken to ensure this including making certain that the cables used in the measurement setup do not

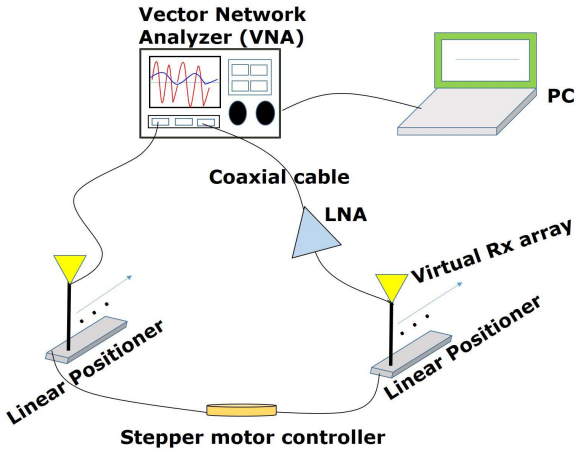


Fig. 4. Channel sounder measurement setup in the warehouse environment.

twist and turn during the positioner movements, and that there were no moving objects, forklift trucks or personnel in the warehouse during the measurement.

## IV. Measurement Data Processing and Results

The channel transfer function of each measured location was extracted from the VNA data. The transfer function can be denoted as $H_{d,s,m,n,f_k}$, where $m = 1...N_T$ and $n = 1...N_R$ respectively denote the Tx and Rx antenna positions in the array, $\{f_k, k = 1...N_F\}$ represents the measured frequencies, $d$ denotes the Tx-Rx separation distance, and $s = 1...N_S$ denote the shadowing position. For our measurement setup, $N_T = 8$, $N_R = 8$, $N_F = 1601$, $N_S$ is 5 and 8 respectively for LOS and NLOS measurements, the set of distances measured are $d = \{5, 10, 15, 20, 25\}$m. The transfer function $H_{d,s,m,n,f_k}$ was transformed to the delay domain by using an inverse Fourier transform with a Hann window to suppress sidelobes. The resulting impulse response is denoted as $h_{d,s,m,n,\tau}$, where

TABLE I
Channel Measurement Parameters

| Parameter | Setting |
|---|---|
| Bandwidth | 6 GHz (2–8 GHz) |
| Transmitted Power | 5 dBm |
| Center frequency, $f_c$ | 5 GHz |
| Total number of channels | 64 |
| Number of sub-carriers | 1601 |
| Delay resolution | 0.167 ns |
| Frequency resolution | 3.74 MHz |
| Maximum path length | 80 m |

TABLE II
Hardware used in the UWB MIMO channel measurement

| Item | Manufacturer | Model No. |
|---|---|---|
| VNA | Agilent | 8720ET |
| LNA | JCA | JCA018-300 |
| Stepper motor control | Velmex | VMX-2 |
| Coaxial cable | Flexco Microwave | FC-195 |

$\tau$ indicates the delay index. The magnitude squared of the impulse response is computed to derive the instantaneous power-delay-profile (PDP), i.e., $P_{d,s,m,n,\tau} = |h_{d,s,m,n,\tau}|^2$. The influence of small-scale fading is removed by averaging the instantaneous PDPs over the 8 x 8 Tx/Rx positions, to obtain the average-power-delay-profile (APDP, $\hat{P}_{d,s,\tau}$).

$$\hat{P}_{d,s,\tau} = \frac{1}{N_T N_R} \sum_{m=1}^{N_T} \sum_{n=1}^{N_R} P_{d,s,m,n,\tau} \quad . \tag{1}$$

Sample APDP plots for both LOS and NLOS measurements at 5 m and 25 m distances are given in [23].

To reduce the influence of noise, we implement a noise-threshold filter, which sets all APDP samples whose magnitude is below a certain threshold to zero. The threshold value is chosen to be 6 dB above the noise floor of the APDP. This noise floor is computed by averaging the energies in all bins with delays shorter than that of the first MPC of the APDP. Also, the APDP was subjected to a delay-gating filter, which eliminates all MPCs whose delays are 60 m or more in excess of the Tx-Rx separation. The APDP is used for RMS delay spread computations, which is further used for model validation in Sec. VI.

### A. Path Gain

Path gain is typically defined as the difference between the received and transmitted power [30]. It has been established through theoretical and practical investigation that the behavior of narrowband and UWB path gains are remarkably different [12], [13], [31]–[35]. An example of this is the fact that for frequency-independent receive antenna area, path gain in narrowband channels is only distance dependent [30], [35], [36]. A generic path gain can be defined as

$$G_L(f,d) = \frac{1}{\Delta f} E\left\{ \int_{f-\Delta f/2}^{f+\Delta f/2} |H(f,d)|^2 df \right\} \quad . \tag{2}$$

where $H(f,d)$ is the channel transfer function. $E\{\cdot\}$ is the expectation taken over the small-scale and large-scale fading. In this case, the frequency range $\Delta f$ is chosen small enough so that the physical parameters such as diffraction coefficients, dielectric constants, etc., can be considered constant within that bandwidth. The modeling can be simplified by considering the distance-dependent path gain $G_L(d)$ to be independent of the frequency-dependent path gain $G_L(f)$, and hence the overall path gain can be written as

$$G_L(f,d) = G_L(d) \cdot G_L(f) \quad . \tag{3}$$

*1) Distance-dependent path gain:* In order to obtain the distance-dependent path gain, we first sum the power in the small-scale averaged PDP (i.e APDP) over all delay bins. The result is commonly referred to as the local mean power ($P^{tot}$). The local mean power is computed separately for measurements at different shadowing points ($s$) and Tx-Rx separation distances ($d$):

$$P_{s,d}^{tot} = \sum_{\tau=1}^{T} \hat{P}_{s,d,\tau} \tag{4}$$

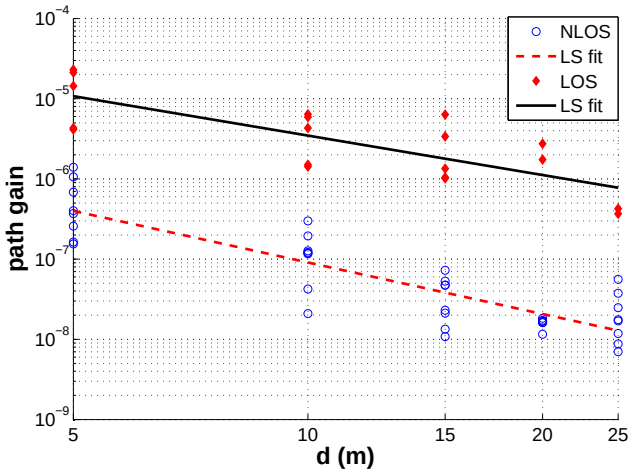


Fig. 5. Distance dependency of the path gain in the LOS and NLOS scenarios.

A relation of local mean power to the distance at each shadowing point would lead the extraction of the path gain component. Following the literature, we use a conventional power law model [30], [36] (see eq. 5);

$$G_L(d) = G_0 - 10 \cdot n \cdot log_{10}\left(\frac{d}{d_0}\right) + S_\sigma \tag{5}$$

where, $n$ is the path gain exponent, $d_0$ is the reference distance (1 m), $G_0$ is the path gain (dB) at the reference distance and $S_\sigma$ is a lognormal distributed random variable describing large-scale variations due to shadowing in the environment. Table III shows the path gain exponent $n$ obtained from LOS and NLOS measurement scenario, while the Fig. 5 shows the scatter plot of the normalized path gain for all distances and shadowing point realization measured. It can be observed that the a linear regression for the scatter plot does show a monotonic dependence of path gain on distance with the slope of the fit corresponding to the path gain exponent experienced in the channel.

TABLE III
EXTRACTED LARGE SCALE CHANNEL PARAMETERS

| | $n$ | $G_0$(dB) | $\kappa$ | $\sigma_s(dB)$ |
|---|---|---|---|---|
| LOS | 1.63 | -38.26 | 1.46 | 2.10 |
| NLOS | 2.14 | -49.06 | 1.46 | 3.16 |

*2) Frequency-dependent path gain:* The frequency-dependence of the path gain ($G_L(f)$) primarily arises from the antenna power area density, gain variations with frequency and additionally from frequency dependence of physical propagation phenomena such as scattering and diffraction. In our model, $G_L(f)$ is expressed as a power-law decay model [37] which in logarithmic form becomes

$$G_L(f) = G_{f_0} - 20 \cdot \kappa \cdot log_{10}\left(\frac{f}{f_{M_c}}\right) \quad . \tag{6}$$

where $\kappa$ is the frequency decay component. $G_{f_0}$ is the power in the lowest frequency sub-band, normalized by the total power. $f_{M_c}$ is the center frequency of each selected sub-band (each sub-band has a bandwidth of 500 MHz with $f_{M_c}$ =

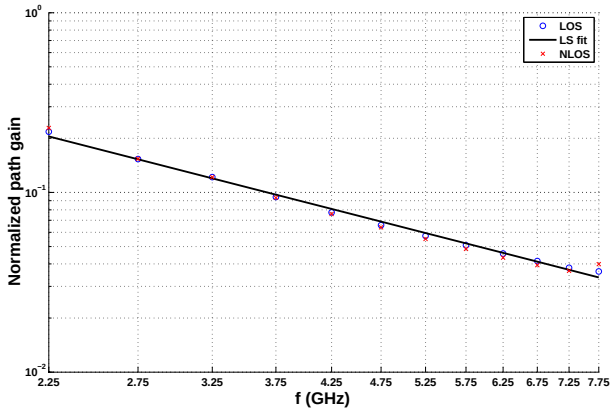


Fig. 6. Frequency dependency of the path gain in the LOS and NLOS scenarios.

2.25 GHz, 2.75 GHz, ... , 7.75 GHz). Though [38] has shown that $\kappa$ can be different for each MPC, we use a "bulk" model in our analysis because we did not have sufficient number of measurement points to extract $\kappa$ for each path separately. The $\kappa$ values obtained for LOS and NLOS scenarios are shown in Table III, while the linear regression fit for the frequency-dependent path gain (dB) as a function of frequency (dB) is shown in Fig. 6. To test the accuracy of the extracted $\kappa$ value, the root-mean-square-error (RMSE) between the measured and the simulated (using eq. 6) frequency-dependent path gain was estimated to be about $-24$ dB. Also, from our calibration measurement in the anechoic chamber with Tx and Rx placed at 1 m separation, $\kappa = 1.1$ was observed. This calibration measurement characterizes the antenna properties in conjunction with the free-space path gain.

### B. Shadowing

Shadowing typically denotes the large-scale fluctuations of the received power in a propagation channel. The logarithmic values of this power deviation observed closely matches a zero-mean Gaussian distribution $N(0, \sigma_s(dB))$, which is standard model for shadowing and has been reported in the literature [39], [40]. This parameter follows the same distribution as well in our analysis and is represented as $S_\sigma$ in our modeling (see eq. 5). The standard deviation $(\sigma_s(dB))$ of this parameter for the LOS and NLOS scenarios are listed in Table III.

## V. Angular Analysis

Directionally resolved channel measurements, and models based on those measurements, are important for the design and simulation of multiantenna systems. In this section, we first extract the delay and direction parameters of the MPCs from the measured channel transfer functions. We perform clustering of the MPCs with similar parameters and develop the stochastic channel models for the LOS and NLOS environments using the intra-cluster and inter-cluster propagation modeling.

### A. MPC parameter extraction using CLEAN

CLEAN is an iterative deconvolution technique first introduced in [41] for the enhancement of the radio astronomical maps of the sky and widely used in microwave and UWB communities as an effective post-processing method for time-domain channel measurements. However, the principle can also be used to extract the delay and direction information from the channel transfer function measurements [14]. The details of the algorithm are available in [42], and not included here for want of space.

Henceforth, $\left(\alpha_i, \tau_i, \phi_i^{DoD}, \phi_i^{DoA}\right)$ shall denote the extracted parameters for the $i^{\text{th}}$ MPC: $\alpha_i$ and $\tau_i$ respectively denote the complex path gain and the delay experienced by the $i^{\text{th}}$ MPC; $\phi_i^{DoD}$ and $\phi_i^{DoA}$ respectively denote the azimuth direction of departure (DoD) and azimuth direction of arrival (DoA) corresponding to the $i^{\text{th}}$ MPC.

### B. Clustering of MPCs

The MPCs tend to be clustered and the clusters usually correspond to the physical scattering objects in the environment. A cluster is defined as a group of MPCs with similar delay, DoA and DoD. Multipath component distance (MCD) is a commonly used distance metric for measuring the similarity of the MPCs. The MCD between the MPCs $i$ and $j$ is defined as [43]

$$MCD_{ij} = \sqrt{MCD_{\tau_{ij}}^2 + MCD_{DoD_{ij}}^2 + MCD_{DoA_{ij}}^2} \quad (7)$$

where,

$$\begin{aligned} MCD_{\tau_{ij}} &= \xi \frac{|\tau_i - \tau_j|}{\Delta\tau_{max}} \frac{\tau_{rms}}{\Delta\tau_{max}} \\ MCD_{DoD_{ij}}^2 &= \frac{1}{4}\left(\cos\phi_i^{DoD} - \cos\phi_j^{DoD}\right)^2 + \frac{1}{4}\left(\sin\phi_i^{DoD} - \sin\phi_j^{DoD}\right)^2 \\ MCD_{DoA_{ij}}^2 &= \frac{1}{4}\left(\cos\phi_i^{DoA} - \cos\phi_j^{DoA}\right)^2 + \frac{1}{4}\left(\sin\phi_i^{DoA} - \sin\phi_j^{DoA}\right)^2 \end{aligned} \quad (8)$$

and where $\tau_{rms}$ is the RMS delay spread and $\Delta\tau_{max}$ is the delay difference between the MPCs, maximized over all pairs of MPCs. $\xi$ is the delay weighting factor, which is chosen by inspection. For the measured data, $\xi = 10$ gave clusters consistent with the environment. Because of the large bandwidth of the measurement setup, the delay information is more accurate and hence more weight is given to the delay information in clustering.

We use the *KPowerMeans* clustering technique, which takes the MPC power into consideration, to group the MPCs into clusters such that the total power weighted MCD of the MPCs from their centroids is minimized [44]. The cluster centroid is defined as the power weighted mean of the parameters of the MPCs in the cluster. For given cluster centroids, the algorithm assigns each MPC to the cluster centroid with the smallest MCD. The cluster centroids are then updated based on the MPC grouping. The cluster centriod computation and the MPC grouping is done iteratively until convergence. The initial cluster centroids are chosen such that they are as far apart as possible.

The *KPowerMeans* algorithm requires as an input the number of clusters $K$. While there are several metrics to find the optimal $K$ based on the compactness of the clusters, like the Calinski–Harabasz index and Davies–Bouldin index [45], they are very sensitive to the outliers in the data. For this reason,

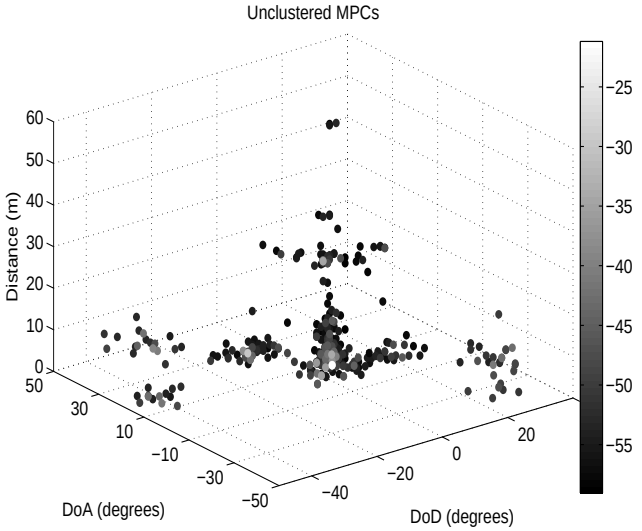


Fig. 7. Scatter plot of the unclustered MPCs. (5 m LOS measurement.)

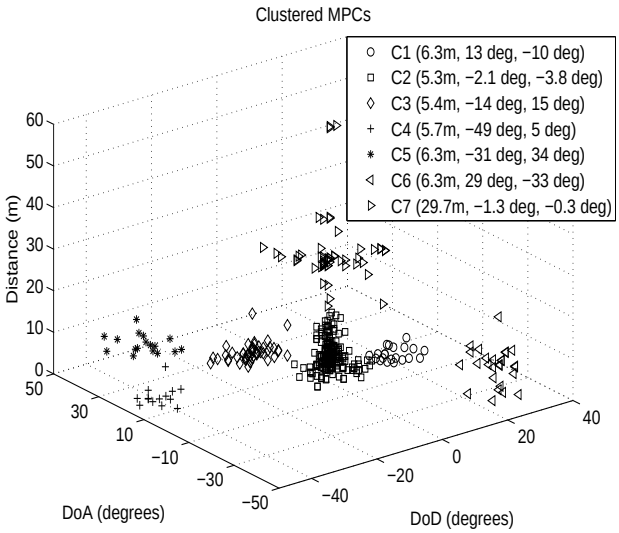


Fig. 8. Clustered MPCs with *KPowerMeans* algorithm. (5 m LOS measurement.)

we use visual inspection to determine the number of clusters for each measurement point: we apply the *KPowerMeans* clustering for a given number of clusters ($2 \leq K \leq 14$) and pick the value of $K$ that gives the visually most compact clusters.

We now present the clustering result for a sample measurement. Fig. 7 plots the delay, DoD and DoA of the MPCs, for a 5 m LOS measurement. The corresponding measurement Tx and Rx locations are shown as TXL3 and RXL3 in Fig. 2. The MPCs are color coded with a scale indicating the path powers in dB scale. Fig. 8 shows the clustered MPCs, obtained using the *KPowerMeans* algorithm. The cluster centroids are shown in the legend. We observed seven clusters for this measurement. Cluster C2 corresponds to the LOS cluster. We observe symmetric clusters with respect to Tx, consistent with

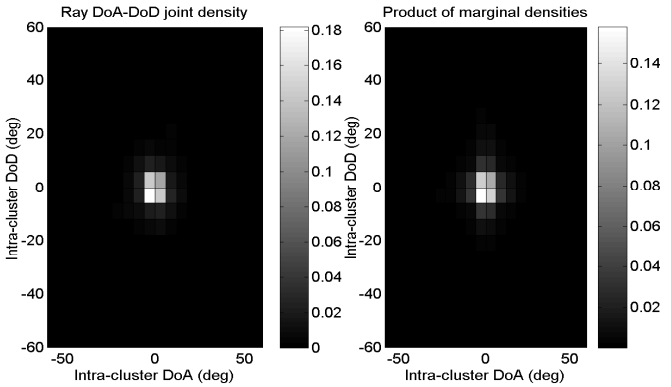


Fig. 9. Figure demonstrating that the intra-cluster DoD and DoA are independent, in the LOS environment.

the environment. Clusters C1, C3, C5 and C6 corresponds to reflections from the concrete pillars and the metal racks on either side of Tx and Rx. Cluster C4 corresponds to reflection from the concrete pillar to the back and to the right of the Tx. Cluster C7 has similar DoD and DoA as that of LOS cluster, but has an excess delay of 24 m compared to the LOS. This corresponds to the reflection from metal racks exactly to the back of the Tx. Please note that for ULAs, the LOS and the back wall reflections have similar DoA/DoD. In our measurements, we observed a significant number of clusters from back wall reflections since the Tx/Rx was placed close to the walls, metal doors etc.

We now develop the channel model for the LOS and NLOS environments separately.

### C. LOS Environment

We first consider the intra-cluster properties of the MPCs, followed by the inter-cluster properties. For all the statistical models developed in the paper, the goodness of the fit is verified by applying the Kolmogorov-Smirnov (K-S) hypothesis test at 5% significance level.

*1) Intra-cluster modeling:* We now develop the model for the ToA, DoD and DoA of the MPCs within each cluster, with respect to the cluster center. [1]

*Dependency of MPC DoD, DoA and ToA:* We first examine the dependency of the MPC ToA, DoD and DoA. Fig. 9 plots the joint density of the MPC DoA and DoD (w.r.t. the cluster center) and compares it with the product of corresponding marginal densities [30]. From visual inspection, we can see that both pdfs are similar and hence it can be concluded that the intra-cluster DoD and DoA are independent. From Fig. 10, which similarly analyzes MPC DoD and ToA, it can be concluded that the intra-cluster ToA and DoD are independent. Similar analysis showed that the intra-cluster DoA and ToA are also independent.

[1]ToA of the cluster center is defined as the smallest ToA of all the MPCs within the cluster. DoD/DoA of cluster center are defined as the power weighted mean DoD/DoA of MPCs within the cluster. The cluster power is defined as the sum of the powers of MPCs within that cluster.

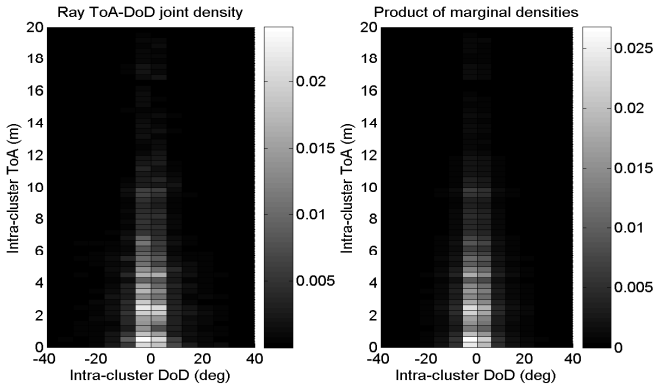


Fig. 10. Figure demonstrating that the intra-cluster DoD and ToA are independent, in the LOS environment.

*Intra-cluster DoD and DoA (w.r.t. cluster center):* The LOS cluster and the NLOS clusters are observed to have slightly different statistics. Figs. 11 and 12 plot the empirical density of the MPC DoA and MPC DoD for the LOS and NLOS cluster respectively, and fit them using a Laplace distribution (with parameters $\mu$ and $b$). It can be seen that the LOS cluster has relatively smaller value of $b$, and hence smaller angular spreads, compared to the NLOS clusters. It was observed that the goodness of the fit was better when the LOS and NLOS clusters was treated separately, comapared to the case where both LOS and NLOS clusters data was combined. Also, the angular spreads observed here are smaller than the angular spread of $20-25^{\circ}$ reported for indoor UWB channel in [14]. Unlike the MIMO measurements in this paper, the indoor measurements in [14] were taken with a SIMO setup and hence the clustering of MPCs was done in ToA and DoA domains only, thus resulting in larger intra-cluster angular spreads.

*Intra-cluster ToA (w.r.t. cluster center):* The delay between the ToAs of successive MPCs is modeled using an exponential mixture distribution. Fig. 13 plots the CCDF for the LOS and NLOS clusters. The mixture probabilities ($\beta$) and the parameter ($\lambda$) of the individual exponential distributions are determined using the expectation maximization (EM) algorithm. It can be seen that the LOS cluster has higher arrival rates compared to NLOS clusters.

*Intra-cluster power decay (Normalized by cluster power):* The power of the MPCs within the cluster decays exponentially with the delay. However, the intra-cluster power decay constant is a function of cluster delay as shown in Fig. 14. It can be seen that the LOS cluster has fast intra-cluster power decay and the far away clusters experience slower intra-cluster power decay. The dependency of the intra-cluster power decay constant on the cluster delay is modeled using a linear function.

*2) Inter-cluster modeling:* We now develop the model for the ToA, DoD and DoA of the cluster centers, with respect to the LOS cluster. The ToA, DoD and DoA of the LOS cluster are completely deterministic: the ToA is given by the Euclidean distance between the Tx and Rx arrays, while DoD and DoA are determined by the relative orientation of Tx and

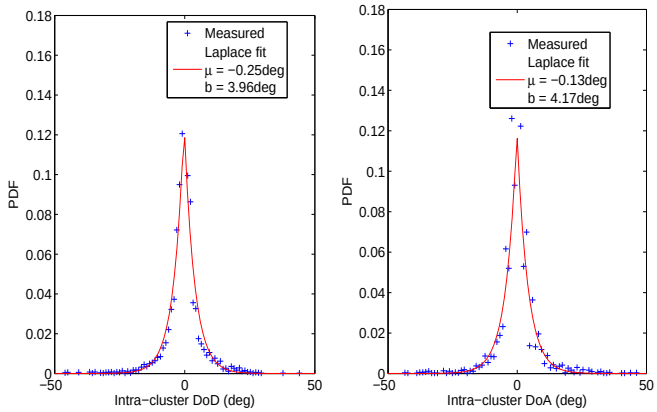


Fig. 11. Intra-cluster DoD and DoA for the LOS cluster, in the LOS environment.

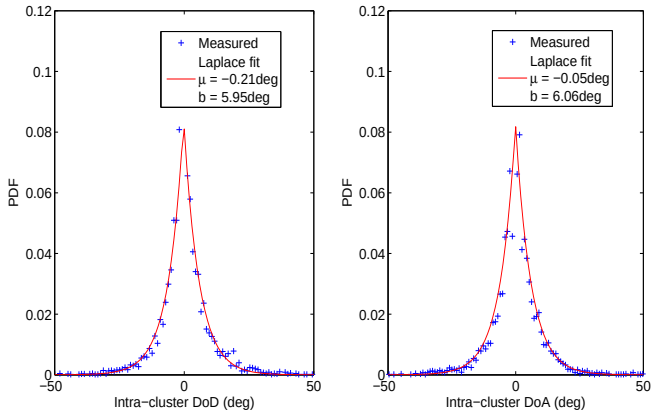


Fig. 12. Intra-cluster DoD and DoA for the NLOS clusters, in the LOS environment.

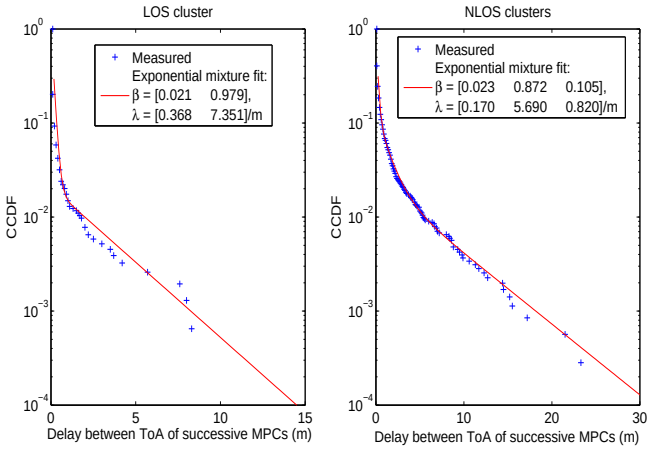


Fig. 13. Intra-cluster ToA modeling for the LOS and NLOS clusters, in the LOS environment.

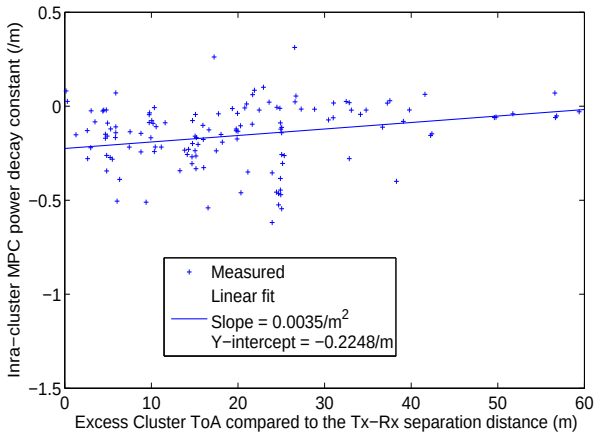


Fig. 14. Intra-cluster power decay constant for different cluster ToA, in the LOS environment.

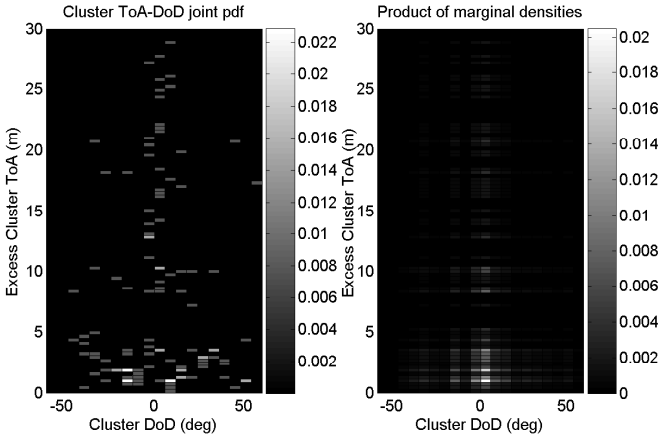


Fig. 16. Figure demonstrating that the cluster DoD and ToA are not independent, in the LOS environment.

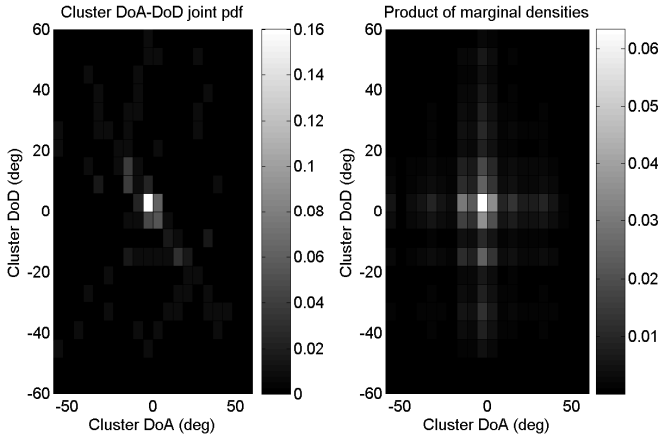


Fig. 15. Figure demonstrating that the cluster DoD and DoA are not independent, in the LOS environment.

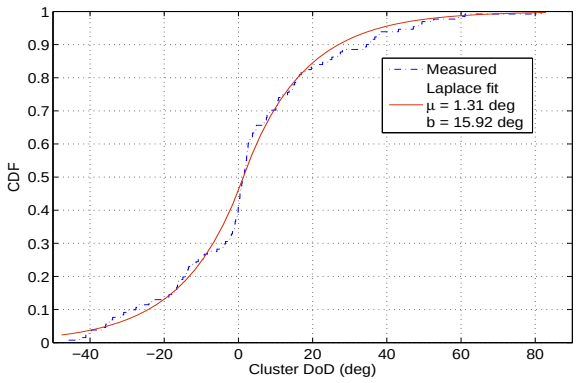


Fig. 17. Cluster DoD modeling in the LOS environment.

Rx antenna arrays. For all the measurements in the paper, the Tx and Rx arrays were aligned and hence the DoD and DoA of the LOS cluster are close to zero degrees.

*Dependency of cluster DoD, DoA and ToA:* Fig. 15 plots the joint density of the cluster DoA and DoD (w.r.t. the LOS cluster) and compares it with the product of the corresponding marginal densities. From visual inspection we can see that both pdfs are very different and hence the cluster DoA and DoD are not independent. Similarly from Fig. 16, we can see that the cluster ToA and DoD are also not independent. Similar observations about dependency of cluster DoD, DoA and ToA were made in [15] for an indoor UWB channel.

*Joint modeling of cluster ToA, DoD and DoA:* The cluster DoD can be approximated using a Laplace distribution as shown in Fig. 17. While both Normal distribution and Laplace distribution were tried to fit the data, the Laplace distribution provided a better fit, which was also verified using the K-S and Akaike's Information Criterion (AIC) hypothesis tests. The relatively large probability mass near zero can be attributed to the backwall reflections. The empirical density function of the cluster DoA, conditioned on the cluster DoD, is shown in Fig. 18. From the measured empirical density, it can be seen that most of the probability mass is concentrated along the diagonals. This is consistent with the propagation environment as we expect most of the propagation through aisles–the principal diagonal represents the single bounce scattering along the aisle and the antidiagonal represents the double bounce scattering along the aisle. To avoid overfitting the data, we use a simple Gaussian mixture distribution to fit the conditional density, *i.e.*, $DoA|DoD \sim 0.8N(-DoD, \sqrt{6^\circ}) + 0.2N(DoD, \sqrt{3^\circ})$, where $N(\mu, \sigma)$ denotes the standard Normal density with mean $\mu$ and variance $\sigma^2$. The simulated conditional density plot using the Gaussian mixture model is shown on the right in Fig. 18. While the proposed model may not be the most accurate representation of the measurements, it captures the dependency of the cluster DoA and DoD with a small number of parameters.

We now model the cluster ToA conditioned on the cluster DoA and DoD. For this, we consider different propagation scenarios. Because of the geometry of the setup and the environment, we observed a significant number of clusters from back wall reflections. For ULAs, the LOS cluster and the back wall refection clusters have very similar cluster DoA

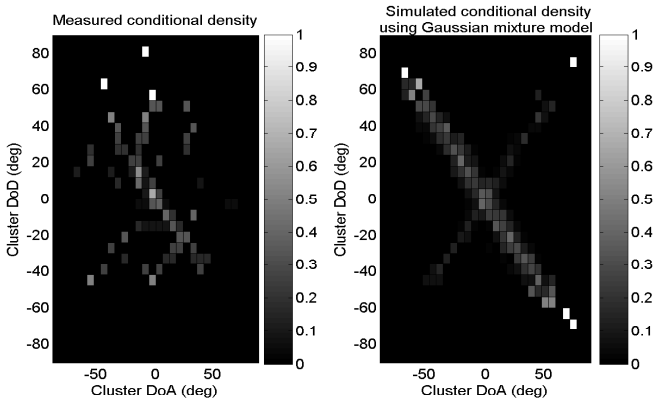


Fig. 18. Figure comparing the measured and simulated conditional density $DoA|DoD$, for the LOS environment.

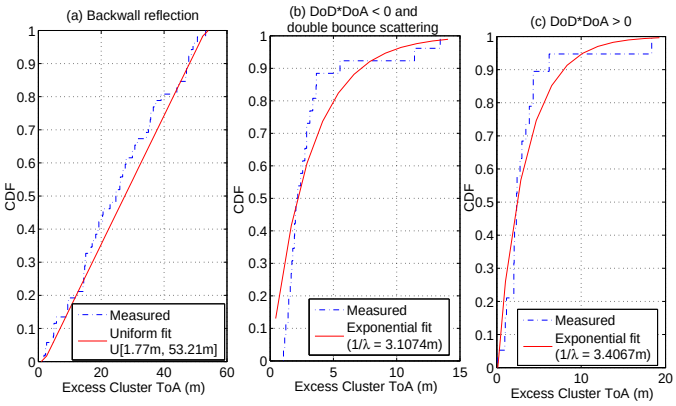


Fig. 19. Modeling the Excess cluster ToA for different propagation scenarios in the LOS environment (a) Backwall reflection (b) Double bounce scattering with $DoD * DoA < 0$ (c) Double bounce scattering with $DoD * DoA > 0$.

and DoD (DoD and DoA are close to 0). For these clusters, the excess cluster ToA, compared to LOS, was observed to be uniformly distributed as shown in Fig. 19 (a). Among the remaining clusters, we further differentiate between single bounce and double bounce scattered clusters. Scattering with more than two bounces will have very weak power in our scenario and hence we ignore them for modeling. For a single bounce scattering clusters, the ToA is a deterministic function of DoA and DoD. If DoA and DoD have same sign (both positive or both negative), we can only have double bounce scattering and the excess cluster ToA, compared to LOS, is modeled using an exponential random variable as shown in Fig. 19 (c); If DoA and DoD have opposite sign, both single bounce and double bounce scattering are possible. For a single bounce, as mentioned earlier, the excess cluster ToA compared to LOS is equal to the deterministic value of $d\frac{\cos(0.5(DoD+DoA))}{\cos(0.5(DoD-DoA))} - d$, where $d$ is the Tx-Rx Euclidean distance. For a double bounce scattering, we model the excess cluster ToA as sum of the excess cluster ToA for a single bounce scattering plus an exponential random variable (Fig. 19 (b)). From the measurements, we observed that $56\%$ of clusters correspond to single bounce scattering.

Hence the excess cluster ToA (w.r.t. LOS) conditioned on the cluster DoA and DoD can be modeled as

$$\begin{aligned}
&\text{ToA}|\text{DoD,DoA} \\
&\sim U[1.77\ m, 53.21\ m], && \text{if } |DoA| < 10^{\circ}, |DoD| < 10^{\circ} \\
&\sim d\frac{\cos(\frac{1}{2}(DoD+DoA))}{\cos(\frac{1}{2}(DoD-DoA))} - d \text{ w.p. } 0.56, && \text{elseif } DoA*DoD<0 \\
&\sim d\frac{\cos(\frac{1}{2}(DoD+DoA))}{\cos(\frac{1}{2}(DoD-DoA))} - d + X_1 \text{ w.p. } 0.44, && \text{elseif } DoA*DoD<0 \\
&\sim X_2, && \text{elseif } DoA*DoD>0
\end{aligned} \tag{9}$$

where $X_1$ and $X_2$ are exponential random variables with means 3.1 m and 3.41 m respectively. [2]

*Cluster power decay:* It is observed that the cluster power decays exponentially with the cluster ToA, and the decay constant is different for different propagation scenarios as shown in Fig. 20. The backwall reflections has the smallest

[2]In both cases, the K-S test passed the exponential hypothesis test only at 1% significance level (fails at standard 5% significance level). Because of the limited sample size and over-fitting issues, we still fit the data with exponential distribution.

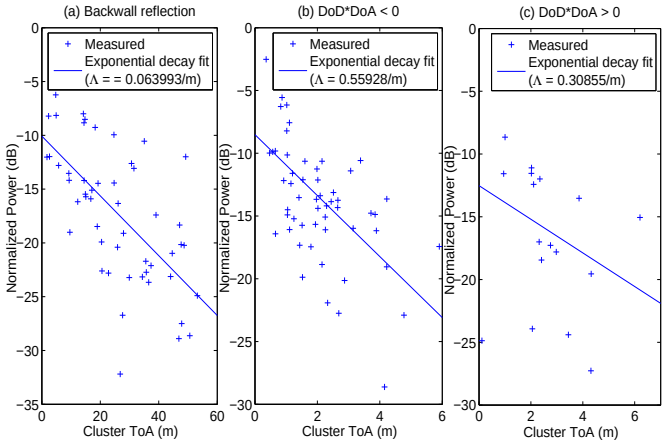


Fig. 20. Inter-cluster power decay for different propagation scenarios in the LOS environment (a) Backwall reflection (b) $DoD * DoA < 0$ (c) $DoD * DoA > 0$.

power decay constant.

*Number of clusters:* The average number of clusters increased with the measurement distance as shown in Fig. 21. The distance dependency is captured by using a linear function. While quadratic function might be a better fit to the data, it can result in over-fitting the data. Since we did not have enough number of observations for each distance to extract the shape of the pdf, we model the number of clusters as a Poison random variable, which is a common assumption in the literature.

*3) LOS channel model:* We now summarize the delay-double directional channel model for the LOS environment. The channel impulse response for a Tx and Rx separated by distance $d$ (in meters) is given by

$$h(\tau,\theta,\phi) = \sum_{k=0}^{K-1}\sum_{l=0}^{L-1} |\alpha_{k,l}| \exp(j\theta_{k,l})\, \delta(\tau - ToA_k - ToA_{k,l}) \times \delta(\theta - DoD_k - DoD_{k,l})\delta(\phi - DoA_k - DoA_{k,l}), \tag{10}$$

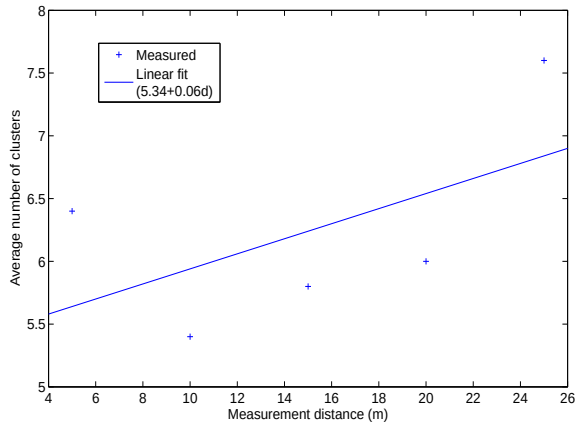


Fig. 21. Average number of clusters as a function of measurement distance in the LOS environment.

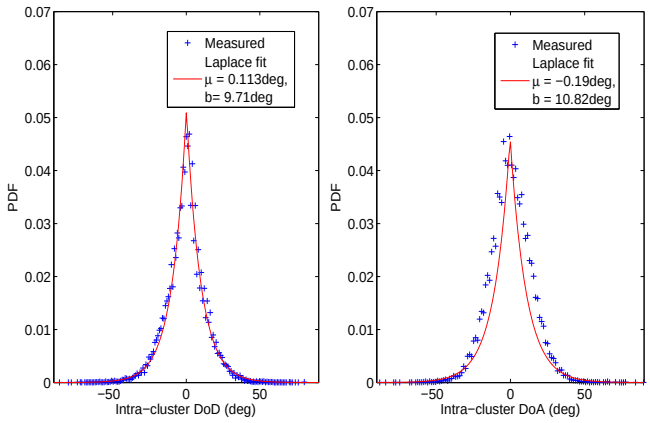


Fig. 22. Intra-cluster DoD and DoA modeling in the NLOS environment.

where the number of clusters is modeled by $K \sim Poisson(5.34 + 0.06d)$.

For the LOS cluster, $ToA_0$ corresponds to the distance between Tx and Rx. $DoD_0$ and $DoA_0$ are determined by the relative orientation of the Tx/Rx arrays. For all subsequent clusters, the cluster centers relative to the LOS cluster ($ToA_k^r \triangleq ToA_k - ToA_0$, $DoD_k^r \triangleq DoD_k - DoD_0$ and $DoA_k^r \triangleq DoA_k - DoA_0$) are modeled as

$$\begin{aligned} DoD_k^r &\sim Laplace(\mu = 1.31^\circ, b = 15.92^\circ), \\ DoA_k^r | DoD_k^r &\sim 0.8N(-DoD_k^r, \sqrt{6^\circ}) + 0.2N(DoD_k^r, \sqrt{3^\circ}) \end{aligned} \tag{11}$$

The conditional density of $ToA_k^r$ given $DoD_k^r$ and $DoA_k^r$ is given in eq. (9).

The intra-cluster ToA, DoA and DoD for the LOS cluster are modeled by:

$$\begin{aligned} &P(ToA_{0,l} - ToA_{0,l-1} > \tau) \\ &\quad = 0.02\exp(-0.37\tau) + 0.98\exp(-7.35\tau) \\ &DoD_{0,l} \sim Laplace(\mu = -0.25^\circ, b = 3.96^\circ) \\ &DoA_{0,l} \sim Laplace(\mu = -0.13^\circ, b = 4.17^\circ) \end{aligned} \tag{12}$$

The intra-cluster ToA, DoA and DoD for the NLOS clusters are modeled by:

$$\begin{aligned} &P(ToA_{k,l} - ToA_{k,l-1} > \tau) \\ &= 0.02\exp(-0.17\tau) + 0.11\exp(-0.82\tau) + 0.87\exp(-5.69\tau) \\ &DoD_{k,l} \sim Laplace(\mu = -0.21^\circ, b = 5.95^\circ) \\ &DoA_{k,l} \sim Laplace(\mu = -0.05^\circ, b = 6.06^\circ) \end{aligned} \tag{13}$$

The MPC power and the phase are modeled by (the small scale fading is not modeled, as the MPCs are resolved in delay, transmit and receive azimuth domains and hence do not expect several unresolvable MPCs in one bin):

$$\begin{aligned} |\alpha_{k,l}|^2 &\propto \exp\left(-\Lambda ToA_k^r\right) \exp\left((-0.22 + 0.0035 ToA_k^r) ToA_{k,l}\right) \\ \theta_{k,l} &\sim U[0, 2\pi] \end{aligned} \tag{14}$$

where the inter-cluster exponential power decay constant ($\Lambda$) is given by

$$\begin{aligned} \Lambda &= 0.064\ m^{-1}, && \text{if } |DoA_k^r| < 10^\circ \text{ and } |DoD_k^r| < 10^\circ \\ &= 0.56\ m^{-1}, && \text{else if } DoA_k^r * DoD_k^r < 0 \\ &= 0.31\ m^{-1}, && \text{else if } DoA_k^r * DoD_k^r > 0 \end{aligned} \tag{15}$$

### D. NLOS Environment

We will now develop the stochastic channel model for the NLOS environment. Most of the observations are very similar to the LOS environment, and hence we only emphasize the key differences from the LOS environment.

*1) Intra-cluster modeling:* As for the LOS environment, the MPC ToA, DoD and DoA are independent. The MPC DoA and DoD are modeled using the Laplace distribution as shown in Fig. 22. The delay between the ToAs of successive MPCs is modeled using exponential mixture distribution as shown in Fig. 23. Unlike the LOS environment, we only have one type of clusters (NLOS clusters) here. The intra-cluster angular spreads here are higher than the angular spreads observed for the NLOS clusters in the LOS environment. It is observed that the MPC power does not monotonically decay with the delay. Rather, it first slightly increases and then decreases as shown in Fig. 24. This soft onset in the intra-cluster MPC power decay was observed in industrial UWB environments as well, where it was modeled as [18].

$$P(\tau) \propto \left(1 - \chi \exp\left(-\frac{\tau}{\gamma_{rise}}\right)\right) \exp\left(-\frac{\tau}{\gamma_{fall}}\right) \tag{16}$$

*2) Inter-cluster modeling:* As observed in LOS environment, the cluster ToA, DoD and DoA are dependent. The dependency is again modeled using the conditional densities. Since there is no physical LOS cluster, we model the cluster DoD, DoA and ToA w.r.t. to the DoD, DoA and ToA corresponding to the geometrical LOS between the Tx and Rx arrays. The cluster DoD can be modeled using the Laplace mixture distribution as shown in Fig. 25. Both Gaussian mixture and Laplace mixture distributions were tried to fit the data and the latter distribution provided a better fit. The conditional

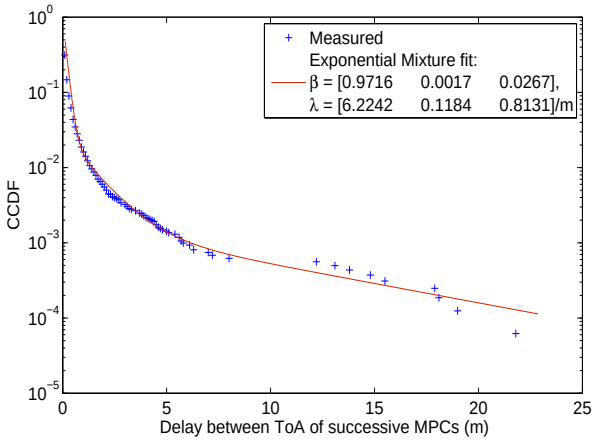


Fig. 23. Intra-cluster ToA modeling in the NLOS environment.

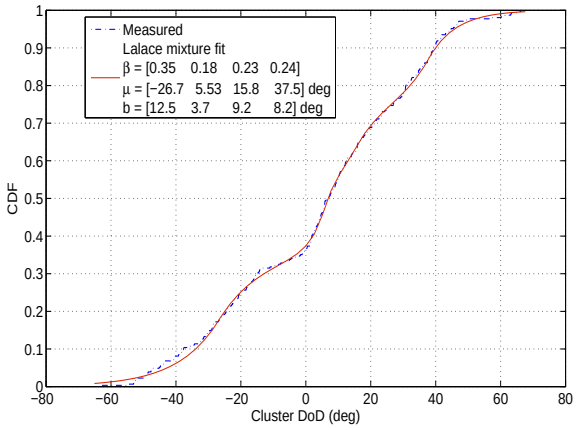


Fig. 25. Cluster DoD modeling in the NLOS environment.

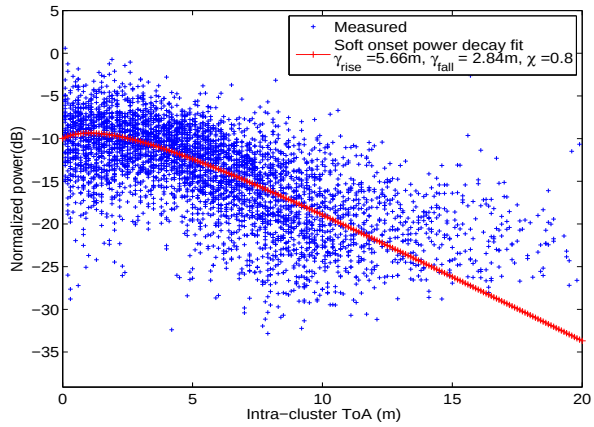


Fig. 24. Intra-cluster power decay modeling in the NLOS environment.

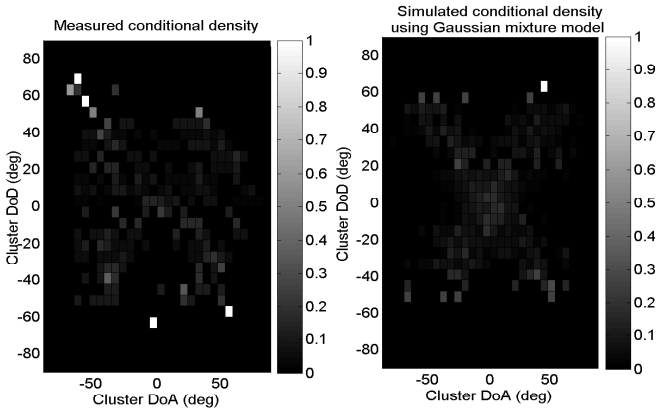


Fig. 26. Figure comparing the measured and simulated conditional density $DoA|DoD$, for the NLOS environment.

density of DoA given DoD is modeled using a Gaussian mixture density, *i.e.*, $DoA|DoD \sim 0.5N(-DoD, \sqrt{15^\circ}) + 0.5N(DoD, \sqrt{15^\circ})$ as shown in Fig 26. As done for the LOS case, the conditional density of excess cluster ToA given cluster DoD and DoA is modeled using Uniform distribution for backwall reflections and Exponential distribution for double bounce scattering, as shown in Fig. 27. The cluster power decays exponentially with the cluster ToA and the power decay constant for different propagation scenarios is given in Fig. 28.

*Number of clusters:* Similar to LOS case, the average number of clusters increased with measurement distance and is modeled using a linear function.

*3) NLOS channel model:* We now summarize the delay-double directional channel model for the NLOS environment. The channel impulse response for a Tx and Rx separated by distance $d$ is given by

$$h(\tau,\theta,\phi) = \sum_{k=1}^{K}\sum_{l=0}^{L-1} |\alpha_{k,l}| \exp(j\theta_{k,l})\, \delta(\tau - ToA_k - ToA_{k,l}) \times \delta(\theta - DoD_k - DoD_{k,l})\delta(\phi - DoA_k - DoA_{k,l}) \quad (17)$$

where the number of clusters is modeled by $K \sim Poi(6.76 + 0.062d)$.

Let $ToA_0 = d$ be the Euclidean distance between Tx and Rx. $DoD_0$ and $DoA_0$ be the DoD and DoA of the geometric LOS between Tx and Rx arrays. The cluster centers relative to the geometric LOS ($ToA_k^r \triangleq ToA_k - ToA_0$, $DoD_k^r \triangleq DoD_k - DoD_0$ and $DoA_k^r \triangleq DoA_k - DoA_0$) are modeled as

$$\begin{aligned} DoD_k^r \sim\ & 0.35Laplace(\mu = -26.7^\circ, b = 12.5^\circ) \\ & + 0.18Laplace(\mu = 5.53^\circ, b = 3.7^\circ) \\ & + 0.23Laplace(\mu = 15.8^\circ, b = 9.2^\circ) \\ & + 0.24Laplace(\mu = 37.5^\circ, b = 8.2^\circ) \\ DoA_k^r|DoD_k^r \sim & 0.5N(-DoD_k^r, \sqrt{15^\circ}) + 0.5N(DoD_k^r, \sqrt{15^\circ}) \end{aligned} \quad (18)$$

The conditional density of $ToA_k^r$ given $DoD_k^r$ and $DoA_k^r$ is given by

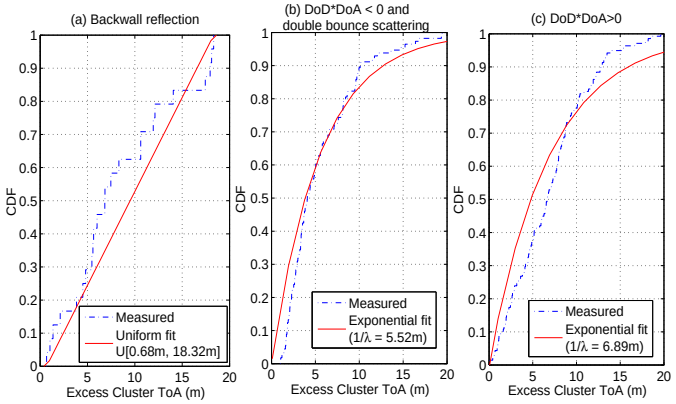


Fig. 27. Modeling the excess cluster ToA for different propagation scenarios in the NLOS environment (a) Backwall reflection (b) Double bounce scattering with $DoD * DoA < 0$ (c) Double bounce scattering with $DoD * DoA > 0$.

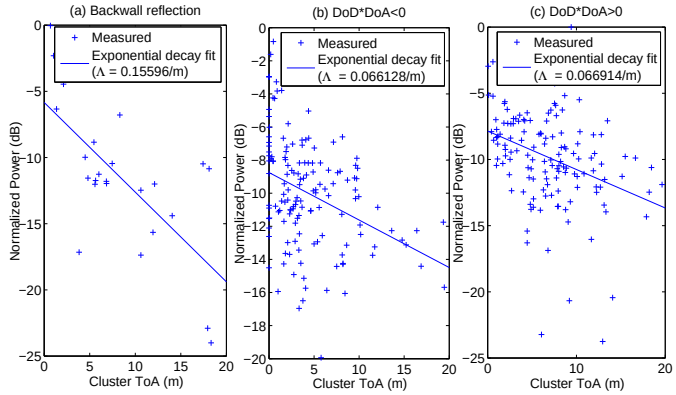


Fig. 28. Inter-cluster power decay for different propagation scenarios in the NLOS environment (a) Backwall reflection (b) $DoD * DoA < 0$ (c) $DoD * DoA > 0$.

$$
\begin{aligned}
&ToA_k^r | DoD_k^r, DoA_k^r \\
&\sim U[0.68\ m, 18.32\ m], && \text{if } |DoA_k^r| < 10^\circ, |DoD_k^r| < 10^\circ \\
&\sim d\frac{\cos(\frac{1}{2}(DoD_k^r + DoA_k^r))}{\cos(\frac{1}{2}(DoD_k^r - DoA_k^r))} - d \text{ w.p. } 0.21, && \text{elseif } DoA_k^r * DoD_k^r < 0 \\
&\sim d\frac{\cos(\frac{1}{2}(DoD_k^r + DoA_k^r))}{\cos(\frac{1}{2}(DoD_k^r - DoA_k^r))} - d + X_1 \text{ w.p. } 0.79, && \text{elseif } DoA_k^r * DoD_k^r < 0 \\
&\sim X_2, && \text{elseif } DoA_k^r * DoD_k^r > 0
\end{aligned} \tag{19}
$$

where $X_1$ and $X_2$ are exponential random variables with mean 5.52 m and 6.89 m respectively. [3]

The intra-cluster ToA, DoD and DoA are modeled by:

$$
\begin{aligned}
P(ToA_{k,l} - ToA_{k,l-1} > \tau) &= 0.9716 \exp(-6.224\tau) \\
&+ 0.0267 \exp(-0.8131\tau) + 0.0017 \exp(-0.1184\tau) \\
DoD_{k,l} &\sim Laplace(\mu = 0.113^\circ, b = 9.71^\circ) \\
DoA_{k,l} &\sim Laplace(\mu = -0.19^\circ, b = 10.82^\circ)
\end{aligned} \tag{20}
$$

[3]For $X_2$ modeling, the K-S test passed the exponential hypothesis test only at 1% significance level (fails at standard 5% significance level). Because of the limited sample size and over-fitting issue, we still fit the data with an exponential distribution.

The MPC power and the phase are modeled by:

$$
\begin{aligned}
|\alpha_{k,l}|^2 &\propto \exp\left(-\Lambda ToA_k^r\right)\left[\left(1 - \chi \exp\left(-\frac{ToA_{k,l}}{\gamma_{rise}}\right)\right)\exp\left(-\frac{ToA_{k,l}}{\gamma_{fall}}\right)\right] \\
\theta_{k,l} &\sim U[0, 2\pi]
\end{aligned} \tag{21}
$$

where $\chi = 0.8$, $\gamma_{rise} = 5.66\ m$, $\gamma_{fall} = 2.84\ m$, and the inter-cluster exponential power decay constant ($\Lambda$) is given by

$$
\begin{aligned}
\Lambda &= 0.156\ m^{-1}, && \text{if } |DoA_k^r| < 10^\circ \text{ and } |DoD_k^r| < 10^\circ \\
&= 0.066\ m^{-1}, && \text{else if } DoA_k^r * DoD_k^r < 0 \\
&= 0.067\ m^{-1}, && \text{else if } DoA_k^r * DoD_k^r > 0
\end{aligned} \tag{22}
$$

## VI. Model Validation

We validate the proposed channel models for the LOS and NLOS environment by comparing the capacity and the RMS delay spreads, from our model to that obtained from the measurement data.

*Synthetic data generation:* For each measurement distance, we generate inter-cluster and intra-cluster ToA, DoD and DoA, and the path weights as per the model given in Sec. V-C3 and V-D3, for the LOS and NLOS channels respectively. The $N_T \times N_R$ channel transfer functions are generated as sum of discrete MPCs, as given below

$$
H(f_k) = \sum_l \alpha_l B_T(f_k, \phi_l) B_R(f_k, \psi_l)^\dagger \exp\left(-j2\pi f_k \tau_l\right), 1 \le k \le N_F \tag{23}
$$

where $\phi_l$, $\psi_l$, $\tau_l$ and $\alpha_l$ respectively denote the DoD, DoA, delay and complex path gain corresponding to the $l^{\text{th}}$ MPC. $B_T(f_k, \phi)$ and $B_R(f_k, \phi)$ are the beampatterns of the Tx and Rx arrays used in the measurements.

Let $H_{syn}(f_k)$ be the synthesized channel transfer function matrix. They are further normalized such that $E\left[\sum_k ||H_{syn}(f_k)||_F^2\right] = N_T N_R N_F$ where the expectation is taken over the realizations of channel. The transfer functions are further multiplied by $\left(\frac{f_k}{f_C}\right)^{-\kappa}$, to model the frequency dependent path loss. ($\tilde{H}_{syn}(f_k) = H_{syn}(f_k)\left(\frac{f_k}{f_C}\right)^{-\kappa}$, $f_C$ is the center frequency.)

*Capacity computation:* The measured channel capacity (bits/sec/Hz) is given by

$$
C_{meas} = \frac{1}{N_F}\sum_k \log_2 \left| I + \frac{1}{N_T N_0} H_{meas}(f_k) H_{meas}(f_k)^\dagger \right| \tag{24}
$$

where $N_0$ is the noise power per sub-carrier, measured from the noise-only region of the channel impulse response, averaged over the measurements.

The synthesized channel capacity for a realization of the channel transfer function, $\tilde{H}_{syn}(f_k)$, is given by

$$
C_{syn} = \frac{1}{N_F}\sum_k \log_2 \left| I + \frac{P}{N_T N_0} \tilde{H}_{syn}(f_k) \tilde{H}_{syn}(f_k)^\dagger \right| \tag{25}
$$

where $P = \frac{1}{N_F}\sum_k ||H_{meas}(f_k)||_F^2$ is the received power per sub-carrier for the corresponding measurement. This is done to ensure that the synthetic data has the same wideband signal-to-noise ratio (SNR) as the measured transfer functions.

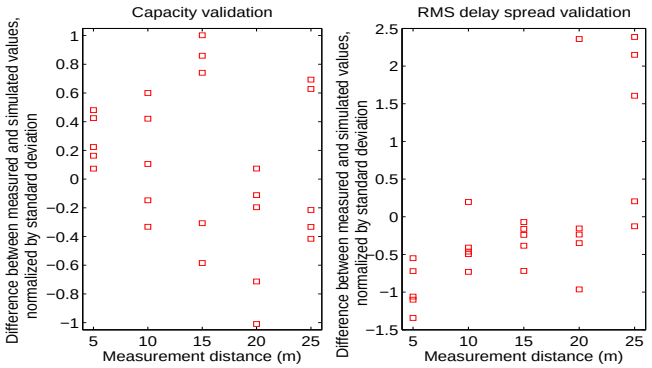


Fig. 29. Capacity and RMS delay spread validation for the LOS channel model.

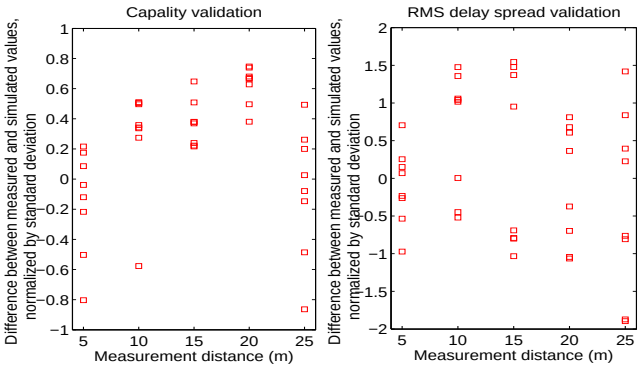


Fig. 30. Capacity and RMS delay spread validation for the NLOS channel model.

*RMS delay spread computation:* RMS delay spread is defined as the second central moment of the average power delay profile (APDP). For each measurement, the APDP is obtained by averaging the absolute square magnitude of the channel impulse response over the $N_T N_R$ measurements.

$$APDP(\tau) = \frac{1}{N_T N_R} \sum_{i=1}^{N_T} \sum_{j=1}^{N_R} |h_{ij}(\tau)|^2 \tag{26}$$

where $h_{ij}(\tau) = IFFT\{H_{ij}(f)\}$ is the channel impulse response between the $i^{th}$ Tx and the $j^{th}$ Rx antenna elements of the array. The noise-threshold filter is applied to the APDP obtained from the measured data, as described in Sec. IV. The RMS delay spread is given by

$$\tau_{rms} = \sqrt{\frac{\int \tau^2 APDP(\tau) d\tau}{\int APDP(\tau) d\tau} - \left(\frac{\int \tau APDP(\tau) d\tau}{\int APDP(\tau) d\tau}\right)^2}. \tag{27}$$

*Capacity and RMS delay spread validation:* We now compare the delay spread and the capacity values computed from the measurements with the synthetic data. For each measurement distance and shadowing point, we have one realization of capacity/delay spread from the measurement, and generate 300 realizations for the synthetic data. We compare the measurement value with the mean value of the synthetic data, normalized by the standard deviation of the synthetic data.

Fig. 29 plots the difference between the mean simulated RMS delay spread/capacity and the measured RMS delay spread/capacity, normalized by the standard deviation of the simulated RMS delay spread/capacity at the given distance, for the LOS environment. It can be seen that the synthetic data agrees reasonably well with the measurements both in terms of capacity and the delay spread: the measured capacity is at-most one standard deviation from the synthetic data and the measured delay spread is within 1.5 standard deviation from the synthetic data, in most cases. The mean values of the channel capacity varies from 80 bits/s/Hz (at Tx-Rx separation distance of 5 m) to 30 bits/s/Hz (at Tx-Rx separation distance of 25 m). The standard deviation of the capacity varied from 10 bits/s/Hz at (at Tx-Rx separation distance of 5 m) to 5 bits/s/Hz (at Tx-Rx separation distance of 25 m). The mean value of the RMS delay spread varied from 16.6 ns to 26.6 ns and the standard deviation of RMS delay spread was around 4 ns. Similar observations hold true even for the NLOS environment as can be seen from Fig. 30. For NLOS case, the mean value of the channel capacity varies from 80 bits/s/Hz (at Tx-Rx separation distance of 5 m) to 40 bits/s/Hz (at Tx-Rx separation distance of 25 m). The standard deviation of the capacity was observed to be between 5-7 bits/s/Hz. The mean and standard deviation values of the RMS delay spreads are 15 ns and 4.3 ns respectively. The capacity captures the angular information and is an indirect validation of the channel model in terms of angular characterization. Unlike the RMS delay spread and channel capacity, the angular spreads cannot be computed directly from the raw channel transfer function measurements.

## VII. Summary and Conclusion

We conducted a measurement campaign in a warehouse environment using a UWB virtual MIMO (8 x 8) antenna array channel sounder setup for LOS and NLOS scenarios. From these measurement data, we obtain a double-directional propagation channel model. The main findings are as follows:

- The distance-dependent path gain coefficient in the LOS and NLOS environments is $n = 1.63$ and $n = 2.14$ respectively.
- The extracted frequency decay components were similar ($\kappa = 1.46$) for both LOS and NLOS scenarios.
- The shadowing was observed to be lognormal distributed with the standard deviation $\sigma(dB) = 2.10$ for the LOS environment and $\sigma(dB) = 3.16$ for the NLOS environment.
- MPCs typically congregate into clusters.
- Intra-cluster analysis showed that the MPC ToA, DoD and DoA are independent. The MPC DoD and DoA fit Laplace distributions and the MPC ToA fit an Exponential mixture distribution. For the LOS environment, the NLOS clusters exhibited higher angular spreads compared to the LOS cluster. The NLOS clusters in the NLOS environment had higher angular spreads than the NLOS clusters in the LOS environment.
- Inter-cluster analysis showed that the cluster ToA, DoD and DoA are dependent. The cluster DoD fits the Laplace

distribution in the LOS environment and the Laplace mixture distribution in the NLOS environment. The conditional DoA (DoA|DoD) can be modeled using a Gaussian mixture distribution for both LOS and NLOS environments. The conditional ToA (ToA|DoD,DoA) fits a Uniform distribution (for backwall reflections), deterministic (for single bounce scattering) and a random Exponential distribution (for double bounce scattering).

- We also observed that the average number of clusters increased with distance. The number of clusters in our measurement was modeled as a Poisson random variable.

From the results and statistics presented in this paper, it is clearly observable that the propagation channel parameters of the warehouse environment are different from those of other environments (indoor [14], industrial [18]) and a specific model, such as provided in this paper, is needed for the system simulations in such an environment.

## ACKNOWLEDGMENT

We would like to thank the USC office of Mailing and Material Management services for their kind permission to measure at the Warehouse. We thank Prof. Xuesong Yang and Umit Bas for their help with the measurement.

## REFERENCES

[1] M. Win and R. Scholtz, "Impulse radio: how it works," *Communications Letters, IEEE*, vol. 2, no. 2, pp. 36–38, 1998.

[2] M. Win, X. Qiu, R. Scholtz, and V.-K. Li, "ATM-based TH-SSMA network for multimedia PCS," *Selected Areas in Communications, IEEE Journal on*, vol. 17, no. 5, pp. 824–836, 1999.

[3] G. Weeks, J. Townsend, and J. Freebersyser, "Performance of hard decision detection for impulse radio," in *Military Communications Conference Proceedings, 1999. MILCOM 1999. IEEE*, vol. 2, 1999, pp. 1201–1206 vol.2.

[4] C. Le Martret and G. Giannakis, "All-digital PAM impulse radio for multiple-access through frequency-selective multipath," in *Global Telecommunications Conference, 2000. GLOBECOM '00. IEEE*, vol. 1, 2000, pp. 77–81 vol.1.

[5] M. Di Benedetto and G. Giancola, *Understanding Ultra Wide Band Radio Fundamentals*, ser. Prentice Hall communications engineering and emerging technologies series. Pearson Education, 2004.

[6] "First report and order 02-48," Federal Communications Commission, Tech. Rep., 2002.

[7] S. Gezici, Z. Tian, G. Giannakis, H. Kobayashi, A. Molisch, H. Poor, and Z. Sahinoglu, "Localization via ultra-wideband radios: a look at positioning aspects for future sensor networks," *Signal Processing Magazine, IEEE*, vol. 22, no. 4, pp. 70–84, 2005.

[8] V. Kristem, A. Molisch, S. Niranjayan, and S. Sangodoyin, "Coherent UWB ranging in the presence of multiuser interference," *Wireless Communications, IEEE Transactions on*, vol. 13, no. 8, pp. 4424–4439, Aug 2014.

[9] M. Win and R. Scholtz, "On the robustness of ultra-wide bandwidth signals in dense multipath environments," *Communications Letters, IEEE*, vol. 2, no. 2, pp. 51–53, 1998.

[10] A. Batra, J. Balakrishnan, G. Aiello, J. Foerster, and A. Dabak, "Design of a multiband OFDM system for realistic UWB channel environments," *Microwave Theory and Techniques, IEEE Transactions on*, vol. 52, no. 9, pp. 2123–2138, Sept 2004.

[11] J. Zhang, P. Orlik, Z. Sahinoglu, A. Molisch, and P. Kinney, "UWB systems for wireless sensor networks," *Proceedings of the IEEE*, vol. 97, no. 2, pp. 313–331, Feb 2009.

[12] C.-C. Chong and S. K. Yong, "A generic statistical-based UWB channel model for high-rise apartments," *Antennas and Propagation, IEEE Transactions on*, vol. 53, no. 8, pp. 2389–2399, 2005.

[13] D. Cassioli, M. Win, and A. Molisch, "The ultra-wideband bandwidth indoor channel:from statistical models to simulations," *IEEE J. Sel. Areas Commun.*, vol. 20, pp. 1247–1257, Aug 2002.

[14] Q. Spencer, B. Jeffs, M. Jensen, and A. Swindlehurst, "Modeling the statistical time and angle of arrival characteristics of an indoor multipath channel," *Selected Areas in Communications, IEEE Journal on*, vol. 18, no. 3, pp. 347–360, March 2000.

[15] T. Zwick, C. Fischer, and W. Wiesbeck, "A stochastic multipath channel model including path directions for indoor environments," *Selected Areas in Communications, IEEE Journal on*, vol. 20, no. 6, pp. 1178–1192, Aug 2002.

[16] B. Kannan and et.al, "UWB channel characterization in outdoor environments," *IEEE 802.15-04-0440-00-004a, Tech. Rep. Doc*, August 2004.

[17] T. Rappaport, S. Seidel, and K. Takamizawa, "Statistical channel impulse response models for factory and open plan building radio communicate system design," *Communications, IEEE Transactions on*, vol. 39, no. 5, pp. 794–807, May 1991.

[18] J. Karedal, S. Wyne, P. Almers, F. Tufvesson, and A. F. Molisch, "A measurement-based statistical model for industrial ultra-wideband channels," *Wireless Communications, IEEE Transactions on*, vol. 6, no. 8, pp. 3028–3037, 2007.

[19] M. Win, F. Ramirez-Mireles, R. Scholtz, and M. Barnes, "Ultra-wide bandwidth (UWB) signal propagation for outdoor wireless communications," in *Vehicular Technology Conference, 1997, IEEE 47th*, vol. 1, May 1997, pp. 251–255 vol.1.

[20] M. Renzo, F. Graziosi, R. Minutolo, M. Montanari, and F. Santucci, "The ultra-wide bandwidth outdoor channel: From measurement campaign to statistical modelling," *Mobile Networks and Applications*, vol. 11, no. 4, pp. 451–467, 2006.

[21] A. Al-Samman, U. Chude-Okonkwo, R. Ngah, and S. Nunoo, "Experimental characterization of an UWB channel in outdoor environment," in *Signal Processing its Applications (CSPA), 2014 IEEE 10th International Colloquium on*, March 2014, pp. 91–94.

[22] T. Santos, J. Karedal, P. Almers, F. Tufvesson, and A. Molisch, "Modeling the ultra-wideband outdoor channel: Measurements and parameter extraction method," *Wireless Communications, IEEE Transactions on*, vol. 9, no. 1, pp. 282–290, January 2010.

[23] S. Sangodoyin, R. He, A. Molisch, V. Kristem, and F. Tufvesson, "Ultrawideband MIMO channel measurements and modeling in a warehouse environment," in *to appear in Communications (ICC), 2015 IEEE International Conference on*, June 2015.

[24] D. Arnitz, U. Muehlmann, and K. Witrisal, "Characterization and modeling of UHF RFID channels for ranging and localization," *Antennas and Propagation, IEEE Transactions on*, vol. 60, no. 5, pp. 2491–2501, May 2012.

[25] F. Mani, F. Quitin, and C. Oestges, "Accuracy of depolarization and delay spread predictions using advanced ray-based modeling in indoor scenarios," *EURASIP Journal on Wireless Communications and Networking*, vol. 2011, no. 1, p. 11, 2011. [Online]. Available: http://jwcn.eurasipjournals.com/content/2011/1/11

[26] "VNA Agilent-Keysight-HP8720ET documentation." [Online]. Available: http://literature.cdn.keysight.com/litweb/pdf/5968-5163E.pdf?id=1000033725:epsg:dow

[27] "Coaxial Cable High frequency RF." [Online]. Available: http://www.flexcomw.com/Products/FC195_files/FC195.pdf

[28] "JCA018-300 Low Noise Amplifier Specification." [Online]. Available: http://www.shungz.com/JCAProducts/JCA_CAT_JCA018_300.pdf

[29] X.-S. Yang, K. T. Ng, S. H. Yeung, and K. F. Man, "Jumping genes multiobjective optimization scheme for planar monopole ultrawideband antenna," *IEEE Transactions on Antennas and Propagation*, vol. 56, pp. 3659–3666, Dec. 2008.

[30] A. Molisch, *Wireless Communications*, ser. Wiley - IEEE. Wiley, 2010.

[31] C.-C. Chong, Y.-E. Kim, S. K. Yong, and S.-S. Lee, "Statistical characterization of the UWB propagation channel in indoor residential environment," *Wireless Communications and Mobile Computing*, vol. 5, no. 5, pp. 503–512, 2005. [Online]. Available: http://dx.doi.org/10.1002/wcm.310

[32] R. Qiu, "A generalized time domain multipath channel and its application in ultra-wideband (UWB) wireless optimal receiver design-part ii: physics-based system analysis," *Wireless Communications, IEEE Transactions on*, vol. 3, no. 6, pp. 2312–2324, Nov 2004.

[33] J. Kunisch and J. Pamp, "Measurement results and modeling aspects for the UWB radio channel," in *Ultra Wideband Systems and Technologies, 2002. Digest of Papers. 2002 IEEE Conference on*. IEEE, 2002, pp. 19–23.

[34] A. Poon and M. Ho, "Indoor multiple-antenna channel characterization from 2 to 8 GHz," in *Communications, 2003. ICC '03. IEEE International Conference on*, vol. 5, May 2003, pp. 3519–3523 vol.5.

[35] A. F. Molisch, "Ultrawideband propagation channels-theory, measurement, and modeling," *IEEE Transactions on Vehicular Technology*, vol. 54, pp. 1528–1545, Sep. 2005.
[36] A. Molisch and et al., "A comprehensive standardized model for ultrawideband propagation channels," *IEEE Trans. Antennas Propag.*, vol. 54, pp. 3151–3166, Nov 2006.
[37] J. Kunisch and J. Pamp, "Measurement results and modeling aspects for the UWB radio channel," in *Ultra Wideband Systems and Technologies, 2002. Digest of Papers. 2002 IEEE Conference on*, May 2002, pp. 19–23.
[38] K. Haneda, A. Richter, and A. Molisch, "Modeling the frequency dependence of ultra-wideband spatio-temporal indoor radio channels," *Antennas and Propagation, IEEE Transactions on*, vol. 60, no. 6, pp. 2940–2950, June 2012.
[39] S. Ghassemzadeh, L. Greenstein, A. Kavcic, T. Sveinsson, and V. Tarokh, "An empirical indoor path loss model for ultra-wideband channels," *Journal of Communications and Networks*, vol. 5, no. 4, pp. 303–308, 2003.
[40] B. Donlan, S. Venkatesh, V. Bharadwaj, R. Buehrer, and J.-A. Tsai, "The ultra-wideband indoor channel," in *Vehicular Technology Conference, 2004. VTC 2004-Spring. 2004 IEEE 59th*, vol. 1, May 2004, pp. 208–212 Vol.1.
[41] J. A. Hogbom, "Aperture synthesis with a non-regular distribution of interferometer baselines," *Astronomy and Astrophysics Supplement Ser*, vol. 15, pp. 417–426, 1974.
[42] V. Kristem and et.al., "Channel measurements and modeling for 3D MIMO outdoor to indoor propagation," *Submitted to Antennas and Propagation, IEEE Transactions on*.
[43] N. Czink, P. Cera, J. Salo, E. Bonek, J.-P. Nuutinen, and J. Ylitalo, "Improving clustering performance using multipath component distance," *Electronics Letters*, vol. 42, no. 1, pp. 33–5–, Jan 2006.
[44] ——, "A framework for automatic clustering of parametric MIMO channel data including path powers," in *Vehicular Technology Conference, 2006. VTC-2006 Fall. 2006 IEEE 64th.* IEEE, 2006, pp. 1–5.
[45] U. Maulik and S. Bandyopadhyay, "Performance evaluation of some clustering algorithms and validity indices," *Pattern Analysis and Machine Intelligence, IEEE Transactions on*, vol. 24, no. 12, pp. 1650–1654, Dec 2002.

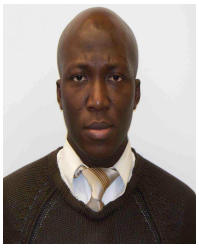

**Seun Sangodoyin** (S'14) received the B.Sc degree in electrical engineering from Oklahoma State University, Stillwater, OK, USA in May 2007 and the M.Sc degree in the same field at the University of Southern California (USC), Los Angeles, CA, USA in 2009. He is currently working towards the Ph.D degree in electrical engineering at the University of Southern California (USC). His research interest includes measurement-based MIMO channel modeling and analysis, multi-antenna systems, UWB MIMO radar, signal processing, estimation theory, body area networks and stochastic dynamical systems. He has been a student member of IEEE for 3 years.

**Vinod Kristem** received the B.Tech. degree in electronics and communications engineering from the National Institute of Technology (NIT), Warangal, India, in 2007 and the M.Engg. degree in telecommunications from the Department of Electrical Communication Engineering, Indian Institute of Science, Bangalore, India in 2009. He is currently working toward his Ph.D. degree with the Department of Electrical Engineering, University of Southern California, Los Angeles. From 2009 to 2011, he was with Broadcom Corp., Bangalore, India. His research interests include Antenna selection in MIMO systems, channel measurements and modeling, UWB ranging and localization.

**Andreas F. Molisch** (S'89-M'95-SM'00-F'05) is a Professor of Electrical Engineering at the University of Southern California, where he is also currently Director of the Communication Sciences Institute. His research interest is wireless communications, with emphasis on wireless propagation channels, multi-antenna systems, ultrawideband signaling and localization, novel cellular architectures, and cooperative communications. He is the author of four books, 16 book chapters, more than 420 journal and conference papers, as well as 80 patents. He is a Fellow of IEEE, AAAS, and IET, Member of the Austrian Academy of Sciences, and recipient of numerous awards.

**Ruisi He** (S'11-M'13) received the B.E. and Ph.D. degrees from Beijing Jiaotong University, Beijing, China, in 2009 and 2015, respectively. Since 2015, Dr. He has been an Associate Professor with the State Key Laboratory of Rail Traffic Control and Safety, Beijing Jiaotong University, Beijing, China. From 2010 to 2014, Dr. He has been a Visiting Scholar in Universidad Politécnica de Madrid, Spain, University of Southern California, USA, and Université Catholique de Louvain, Belgium. His current research interests include measurement and modeling of wireless propagation channels, machine learning and clustering analysis in wireless communications, vehicular and high-speed railway communications, 5G massive MIMO and high frequency communication techniques.

**Fredrik Tufvesson** received his Ph.D. in 2000 from Lund University in Sweden. After two years at a startup company, he joined the department of Electrical and Information Technology at Lund University, where he is now professor of radio systems. His main research interests are channel modelling, measurements and characterization for wireless communication, with applications in various areas such as massive MIMO, UWB, mm wave communication, distributed antenna systems, radio based positioning and vehicular communication. Fredrik has authored around 60 journal papers and 120 conference papers, recently he got the Neal Shepherd Memorial Award for the best propagation paper in IEEE Transactions on Vehicular Technology.

**Hatim Behairy** is the director of the National Center for Electronics and Photonics Technology at King Abdulaziz City for science and Technology in Riyadh, Saudi Arabia. He has more than 15 years of experience in both industry and academia in Saudi Arabia and North America relating to telecommunications, software development, and management. He received his B.Sc in Computer Engineering in 1995 from King Saud University, Riyadh, Saudi Arabia. He received the Msc degree in Electrical Engineering in 1997, and the Ph.D. degree in Information Technology in 2002 from George Mason University, Virginia, USA. His research results have been published in leading journals and conferences. He worked extensively, and he is still working, on the design of new error correction coding techniques for next-generation broadband wireless communication systems, using turbo-coding principles. His research interests are in Secure communication systems, UWB systems.